Materials Science and Engineering A, Vol. 223, 1997, pp. 146–157

Inoculation of Steel Welds With Non–Metallic Particles

J. M. Gregg, H. K. D. H. Bhadeshia and L.–E. Svensson†

University of Cambridge/JRDC
Department of Materials Science and Metallurgy
Pembroke Street, Cambridge CB2 3QZ, U.K.

Central Research Laboratories
ESAB AB, Gothenburg, Sweden

ABSTRACT

Two series of experimental submerged arc welds have been produced, in which additions of titanium-rich and tungsten-rich powders have been made to the flux. Such additions have caused variations in weld composition. Weld microstructures were observed to become more intragranularly dominated with increases in either titanium or tungsten. In titanium welds, microstructural changes were due to changes in inclusion mineralogy and consequently to nucleating potential, as well as to matrix hardenability. In tungsten welds, microstructural variations were solely due to the effects of tungsten in solution.

INTRODUCTION

A series of experiments have recently been reported [1, 2] in which an attempt was made to identify the non–metallic inclusions which are useful as heterogeneous nucleation sites for acicular ferrite in steels. Some of these experiments involved the pressure bonding of pure ceramic compounds to steel; the resulting composite was then transformed to see whether nucleation was enhanced at the ceramic/steel interface when compared with the bulk of the steel. These experiments proved capable of ranking the ferrite–nucleation potency of a variety of non–metallic compounds, and formed the basis of further trials [3] in which the compounds were added directly to steel melts, which were stirred and solidified rapidly to produce inoculated steels containing uniform dispersions of particles. The experiments proved successful: the particles were not on the whole adversely affected by the steel melt, and it was found possible to stimulate the formation of ferrite on the added particles.

The work confirmed the potency of many of particles popularly believed to be effective in stimulating acicular ferrite, and others which have never been studied before. The purpose of the present work was to extend the research by inoculating steel welds with selected compounds. Attempts were therefore made to add titanium–rich compounds, and unusually, some tungsten oxide (which has been found to be a potent nucleant in the pressure bonding experiments [1, 2]).

EXPERIMENTAL

Two series of experimental 0.5 m long submerged arc welds were produced, with weld geometry as shown in Fig.1. The welding conditions for all the welds are summarised in Table 1. The first series of welds (B–D) involved variations in titanium and the second (E–G) in tungsten. A control weld (A) was also made for comparison purposes, without any deliberate mineral addition (Table 2). The welding wire used was ESAB AB Autrod 12.22. The exact weld chemistries formed by various powder additions are discussed in the following sections.

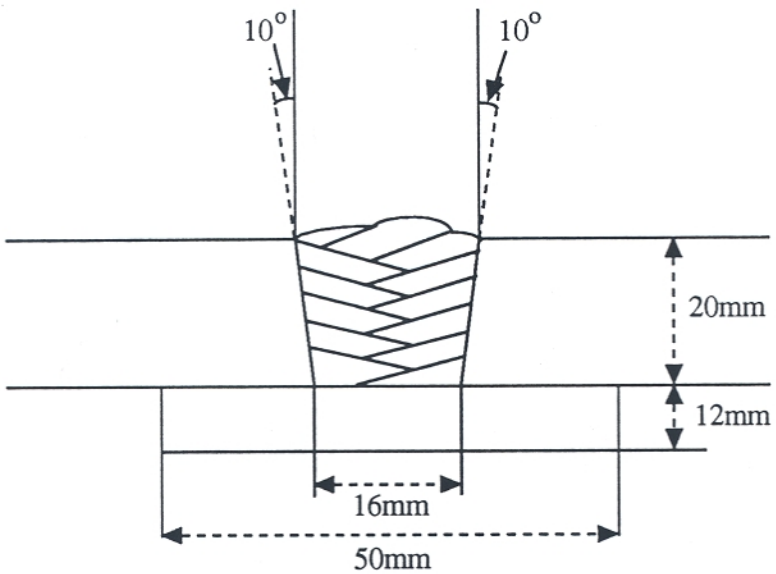

Figure 1 Geometry of the experimental welds produced

FeSi	SiMn	SiO_2	Al_2O_3	MgO	AlSi	CaF_2
1.7	2	5	15.9	43.6	5	26.8

Table 2 Composition of the basic flux to which powder additions were made. Concentrations shown are in wt%

TITANIUM–RICH ADDITIONS

Weld A was produced using the unmodified flux (Table 2). Titanium was introduced differently in each of the other welds in the titanium series, but, in each case the powder added constituted 4 wt% of the flux composition. Additions were as follows: flux rich in TiO_2 powder was used to produce Weld B; FeTi powder was added to the flux to produce

Weld	Flux used	ϕ /mm	Interpass Temp. /°C	Current Type	Voltage /Volts	Current /Amps	Speed /m/h
A	Basic Flux	4.0	175 ± 25	DC+	29	580	33
B	Basic Flux + TiO_2 powder	4.0	175 ± 25	DC+	29	580	33
C	Basic Flux + FeTi powder	4.0	175 ± 25	DC+	29	580	33
D	Basic Flux + Ti powder	4.0	175 ± 25	DC+	31	580	33
E	Basic Flux + WO_3 powder	4.0	175 ± 25	DC+	29	580	33
F	Basic Flux + W powder	4.0	175 ± 25	DC+	29	580	33
G	Basic Flux + FeW powder	4.0	175 ± 25	DC+	29	580	33

Table 1 Welding conditions for experimental submerged arc welds.

Weld C; Ti–powder was added to the flux for Weld D. The weld compositions thus achieved are shown in Table 3. The titanium concentration increases across the series A→D, without significant variations in the C, Si or Mn concentrations.

Weld	C	Si	Mn	Al	Ti	O	N
A	0.075	0.36	1.26	0.012	0.003	280	48
B	0.082	0.49	1.29	0.015	0.019	218	64
C	0.090	0.70	1.34	0.028	0.081	204	90
D	0.091	0.73	1.28	0.030	0.124	134	64

Table 3 Composition of the titanium series welds. Concentrations are given in wt.%, with O and N given in parts per million by weight.

As–Deposited Microstructure

The welds were sectioned perpendicular to the welding direction and the top bead isolated for metallographic examination. Because of the fine scale, the microstructures had to be characterised using scanning electron microscopy. Figures 2–5 show that an increase in the titanium concentration seems to lead to a corresponding increase in the acicular ferrite content. At the same time, the amount of grain boundary allotriomorphic ferrite and Widmanstätten ferrite was observed to decrease, eventually with complete elimination

from the microstructure.

Variations in Widmanstätten ferrite are expected with changes in the frequency of intragranular nucleation events. Widmanstätten ferrite grows from the austenite grain surfaces and its growth can be stifled by impingement with intraganularly nucleated acicular ferrite. If the latter forms more rapidly, then the fraction of Widmanstätten ferrite is expected to decrease. Thus the reduction of Widmanstätten ferrite may be explained by an increase in the nucleation potency of the inclusions, as titanium levels are increased. It is more surprising that the amount of allotriomorphic ferrite is reduced since its growth starts from a significantly higher temperature than acicular ferrite. It is possible that, in addition to any nucleation effect due to increased levels of titanium–rich phases in the inclusions, some of the titanium is retained in solution, enhancing hardenability, which in turn is reflected in the reduced allotriomorphic ferrite content.

Kluken and Grong [4] have developed methods to estimate the constitution of inclusions in steel welds, by sequentially distributing the oxygen and nitrogen, beginning with the most potent oxidisers *etc.* . The method has been stated explicitly in [5] and is used here to estimate the likely constituents of the non–metallic inclusions present in the weld series, and also to examine the likelihood that excess titanium may be present in solution in the high titanium welds. The results of the analysis are presented in Table 4.

Weld	Allocation of Oxygen /ppmwt				Allocation of Titanium /ppmwt		
	Al_2O_3	Ti_2O_3	MnO	SiO_2	TiN	Ti_2O_3	Ti in solution
A	107	15	80	78	0	30	0
B	121	95	1	1	0	190	0
C	173	31	0	0	308	63	439
D	181	0	0	0	219	0	1021

Table 4 Calculated allocation of titanium and oxygen to mineral groups in non–metallic inclusions

As can be seen from the table, according to calculations, the levels of titanium present in welds C and D were such that excess titanium would indeed be present in solution. Despite being a ferrite stabiliser [6], titanium in solution has been observed to cause a dramatic increase in steel hardenability [7].

Despite this hardenability effect, it should be noted that areas of bainite could readily

be observed in Weld C, but not in Weld D. Bainite and acicular ferrite compete directly as transformation products – their mechanism of transformation being the same, save that bainite nucleates from planar grain boundaries, and acicular ferrite nucleates from point sources within grains. The reduction of bainite in Weld D implies that intragranular nucleation has been enhanced over grain boundary nucleation. It seems, from metallographic observations alone, that the role of titanium is therefore two–fold:

(i) Its presence in solution increases the hardenability of the weld metal.

(ii) It causes greater levels of intragranular over grain boundary nucleation – probably attributable to changes in the nucleation potency of non–metallic inclusions.

Examination of Inclusions

Carbon extraction replicas were prepared for each of the welds in this titanium–series. These replicas allowed examination of the weld inclusions and analysis of their chemical, mineralogical, and morphological information.

As expected, EDX microanalysis revealed that increased titanium led to inclusions richer in Ti (Fig.6). More profound chemical differences were also identified. Figures 7–9 show that for Welds A & B (the titanium–poor welds) the levels of silicon, aluminium and manganese were reasonably constant in all inclusions examined (*i.e.* there were specific peaks in the distributions of chemical concentrations). As the level of titanium increased, the manganese and silicon concentrations dropped, and the distribution of aluminium within the inclusions became more homogeneous.

The change from specific concentrations of aluminium in the low titanium welds to a more homogeneous concentration distribution implies a change in the state of aluminium in the non–metallic inclusions. This change, accompanied by the removal of silicon and manganese, is consistent with a mineralogical change from manganese–aluminium oxide, or manganese–aluminium silicate–rich inclusions, to those containing varying levels of alumina as a phase component in the inclusion. The likelihood of such mineralogical changes is supported by the calculated results shown in Table 4.

Diffraction patterns taken from crystalline inclusions revealed the presence of MnS (only in Ti–poor welds – Fig.10), Al_2O_3 (apparently in several forms, in all welds – Fig.12, Fig.13), TiX (where X=C, N, or O, in all welds – Fig.11), $MnAl_2O_4$ (in Weld D only, Fig.14) and a sulphide phase suspected to be a copper sulphide (in all welds, Fig.15). Crystalline silicate was never observed, presumably because the silicate was present in its glassy form.

Information from specific diffraction patterns is summarised in Table 5. The miner-

alogies present are largely the same across the weld series. However, the relative amounts of each mineral phase varies – as inferred from chemical changes, and also from qualitative morphological observations:

Often, inclusions which were demonstrated to contain a lot of Ti by microanalysis, showed angular, cuboidal shapes consistent with TiN. The number of such cuboidal inclusions increased across the weld series, but showed a dramatic jump between Weld B and Weld C (Figures 16 and 17). This sudden increase in levels of TiN is supported by the calculated results in Table 4.

Thin–foil Examination

Although the levels of titanium in the weld metals were quite low, an attempt to demonstrate the presence of titanium in solution in the matrix steel was made, by preparing thin–foils for matrix microanalysis. Unfortunately, the concentration of Ti was below the resolution of the EDX system employed. However, three cases of detectable titanium levels in matrix steel were recorded – all for the titanium–rich weld, Weld D.

Weld	Observed			Likely Phase	Likely		Calculated		
	d_1	d_2	$d_1 \hat{} d_2$		$(hkl)_1$	$(hkl)_2$	d_1	d_2	$d_1 \hat{} d_2$
Weld A	2.7Å	1.6Å	72°	MnS	(311)	(020)	2.6Å	1.6Å	72°
Weld A	2.4Å	1.45Å	88°	γ-Al_2O_3	(311)	$(11\bar{5})$	2.4Å	1.5Å	87°
Weld A	2.3Å	2.0Å	54°	TiX	(111)	(200)	2.4Å	2.1Å	54.7°
Weld B	1.9Å	1.2Å	90°	Cu_xS					
Weld B	2.4Å	2.35Å	60°	α-Al_2O_3	(110)	$(2\bar{1}0)$	2.4Å	2.4Å	60°
Weld B	1.3Å	1.3Å	60°	TiX	(311)	$(1\bar{1}3)$	1.28Å	1.28Å	63°
Weld B	3.7Å	3.7Å	68°	Form of Al_2O_3					
Weld B	2.7Å	8.5Å	78°	Complex Ti-oxide					
Weld B	2.0Å	2.0Å	82°	Form of Al_2O_3					
Weld C	2.6Å	2.6Å	70°	TiX	(111)	$(1\bar{1}1)$	2.4Å	2.4Å	70.5°
Weld C	2.2Å	2.2Å	90°	TiX	(020)	(200)	2.1Å	2.1Å	90°
Weld C	2.3Å	1.4Å	90°	Cu_xS					
Weld C	2.6Å	2.6Å	65°	α-Al_2O_3	(104)	(014)	2.6Å	2.6Å	60°
Weld C	2.7Å	4.2Å	86°	γ-Al_2O_3	(111)	$(2\bar{2}0)$	2.8Å	4.56Å	90°
Weld C	3.6Å	3.6Å	88°	α-Al_2O_3	(012)	$(10\bar{2})$	3.5Å	3.5Å	86°
Weld C	3.0Å	3.0Å	90°	$MnAl_2O_4$	(220)	$(2\bar{2}0)$	2.9Å	2.9Å	90°
Weld D	4.8Å	4.7Å	70°	γ-Al_2O_3	(111)	$(1\bar{1}1)$	4.56Å	4.56Å	70.5°
Weld D	2.1Å	2.1Å	70.5°	Cu_xS					
Weld D	2.9Å	3.1Å	90°	$MnAl_2O_4$	(220)	$(2\bar{2}0)$	2.9Å	2.9Å	90°
Weld D	2.5Å	1.5Å	90°	TiX	(111)	$(2\bar{2}0)$	2.4Å	1.5Å	90°
Weld D	2.1Å	2.1Å	70°	Cu_xS					

Table 5 Summary of the data obtained from diffraction patterns taken from particles in the titanium series of welds.

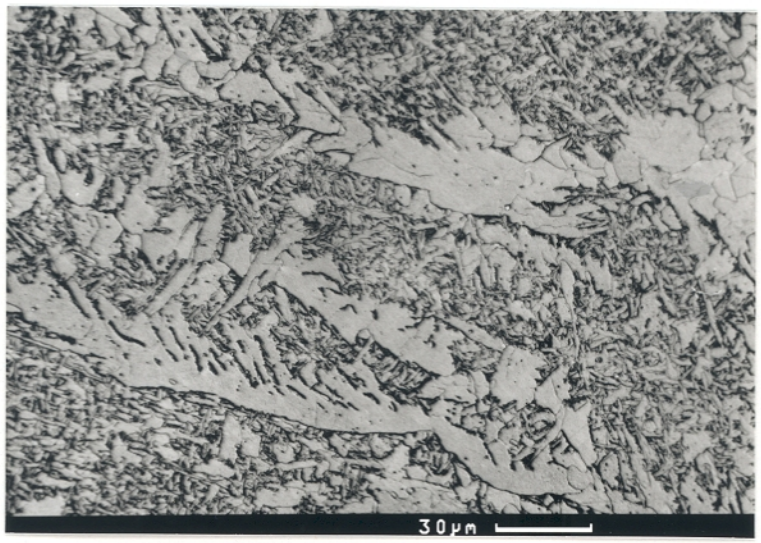

Figure 2 SEM micrograph of the as–deposited microstructure in Weld A (low titanium weld).

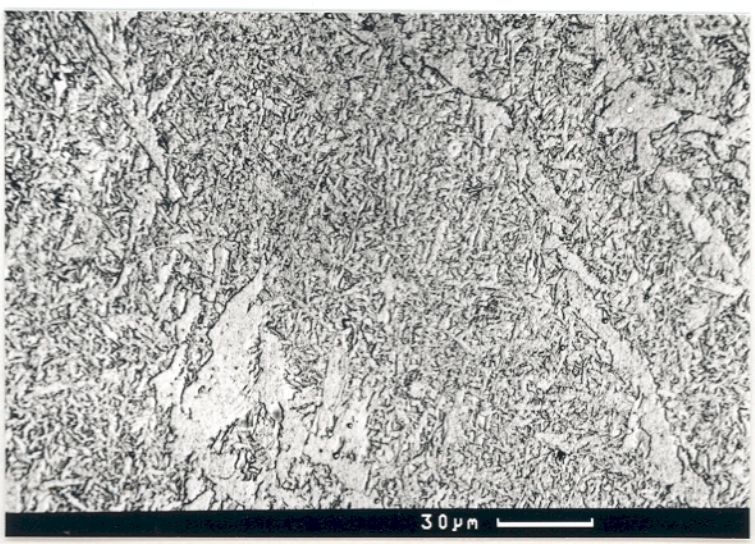

Figure 3 SEM micrograph of the as–deposited microstructure in Weld B.

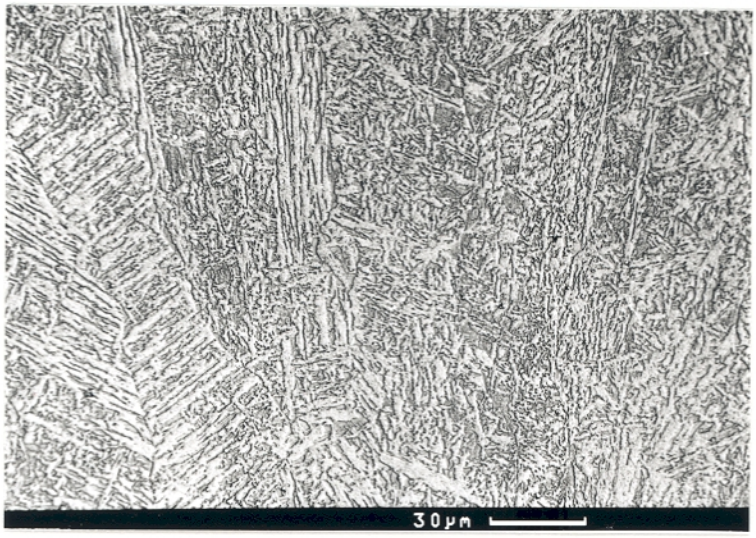

Figure 4 SEM micrograph of the as–deposited microstructure in Weld C.

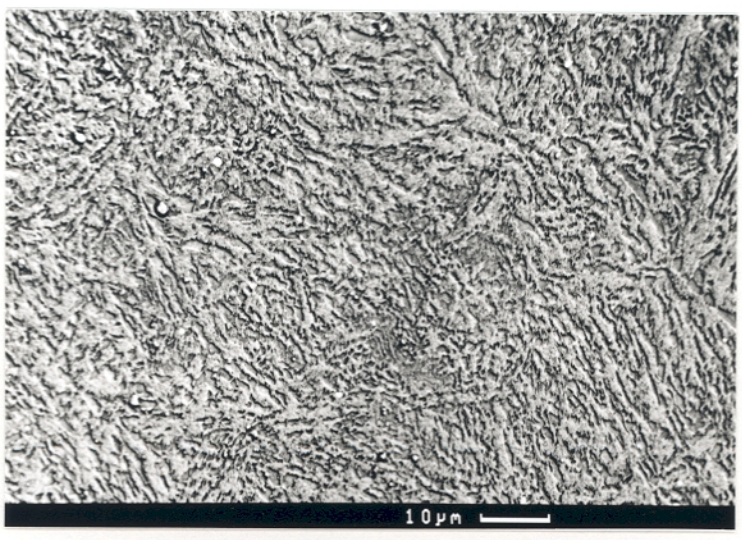

Figure 5 SEM micrograph of the as–deposited microstructure in Weld D (titanium–rich weld).

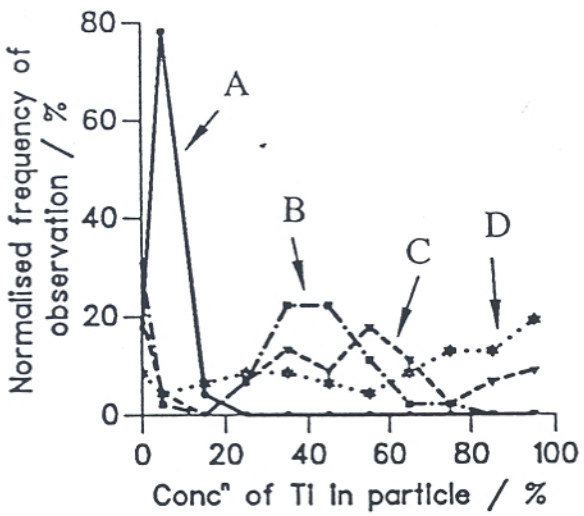

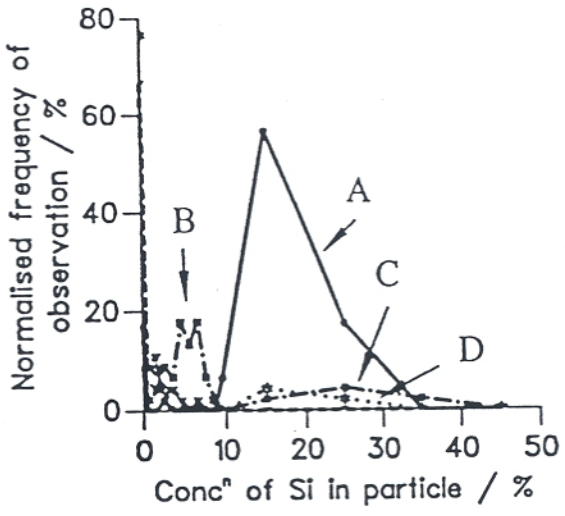

Figure 6 (left) Titanium concentration distribution in inclusions across the titanium–weld series. Concentrations are in wt% .
Figure 7 (right) Silicon concentration distribution in inclusions across the titanium–weld series. Concentrations are in wt% .

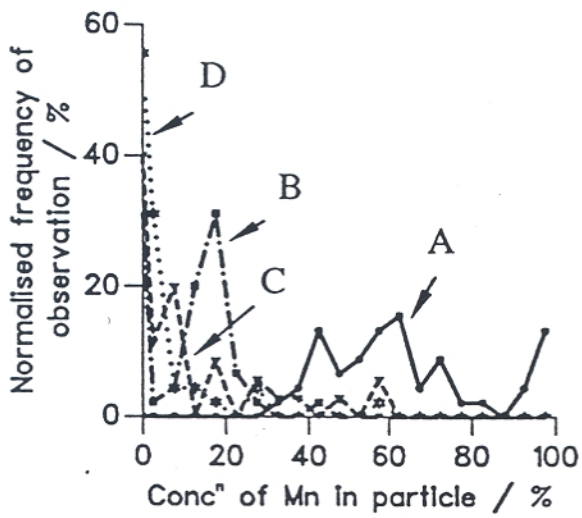

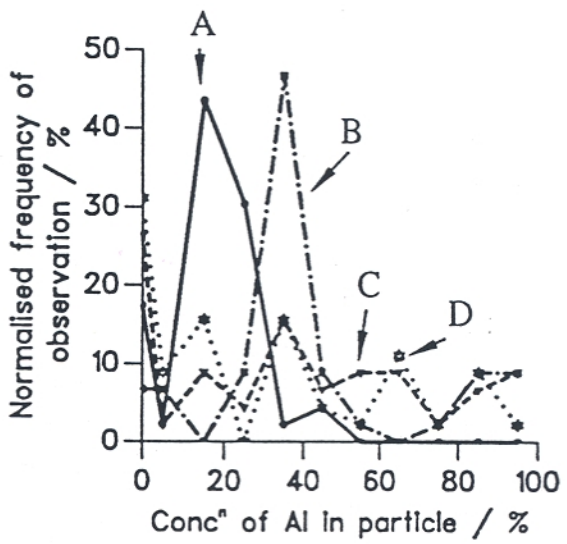

Figure 8 (left) Manganese concentration distribution in inclusions across the titanium–weld series. Concentrations are in wt% .
Figure 9 (right) Aluminium concentration distribution in inclusions across the titanium–weld series. Concentrations are in wt% .

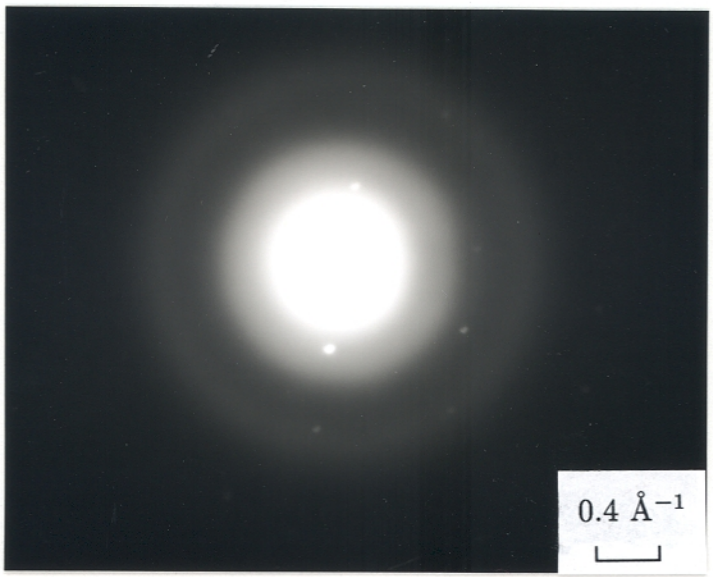

Figure 10 Diffraction pattern from part of an inclusion in Weld A. It is consistent with MnS. This phase does not appear in the more titanium–rich welds.

Figure 11 Diffraction patterns consistent with TiX were found in all the welds, but become more common with increases in titanium addition.

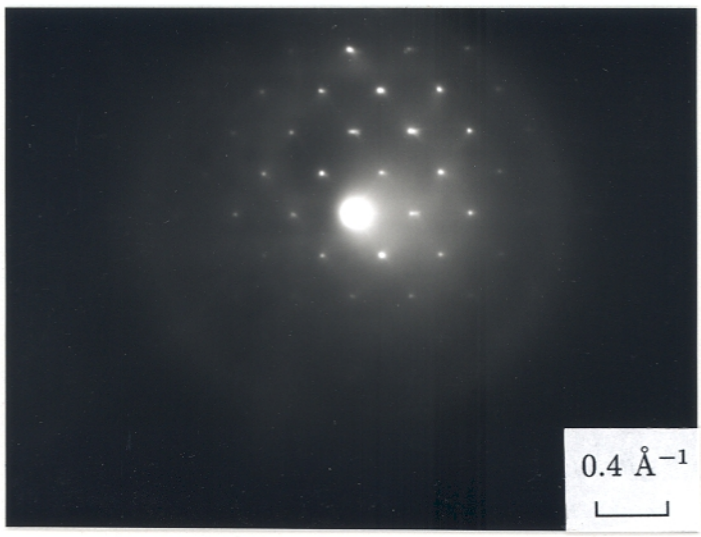

Figure 12 Different alumina types were distinguished in particles across the titanium–weld series. This pattern is consistent with γ-Al_2O_3.

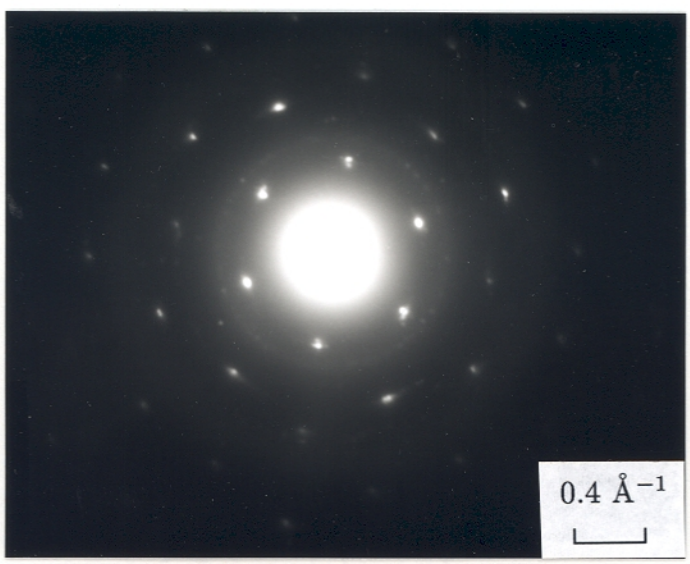

Figure 13 This diffraction pattern is consistent with α-Al_2O_3.

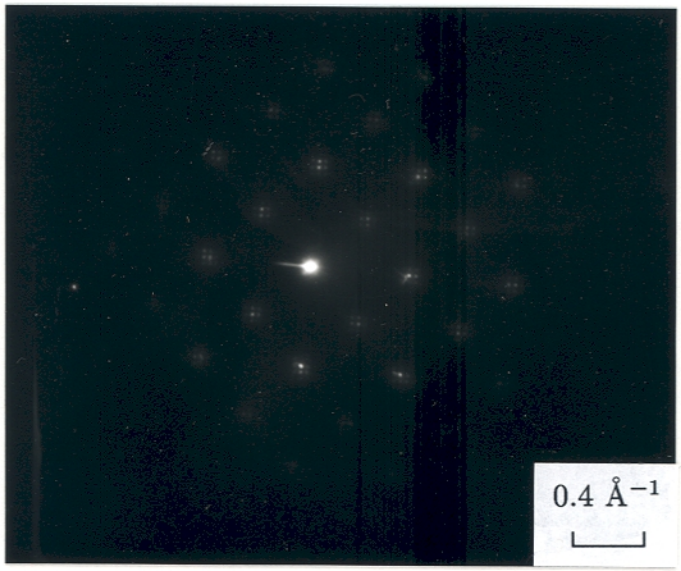

Figure 14 Several diffraction patterns were found which corresponded well with $MnAl_2O_4$. Here some super–periodicity is illustrated by the numerous satellite spots.

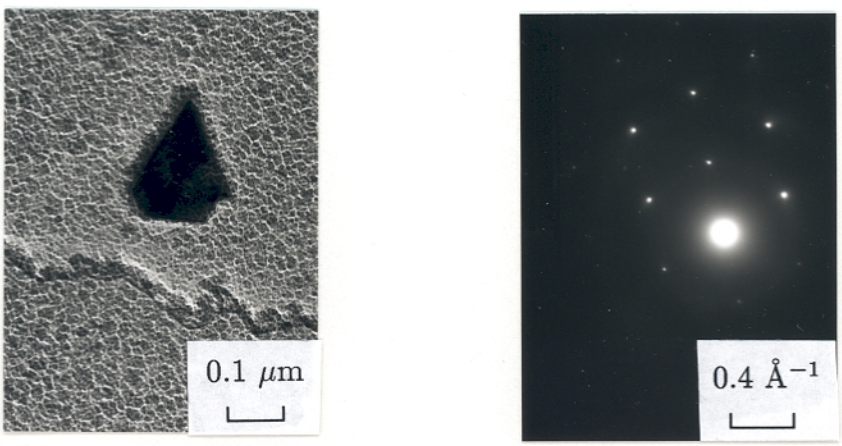

(a) **(b)**

Figure 15 **(a)** A sulphur–rich phase was frequently observed, which did not contain significant levels of manganese. It was suspected that this phase was a copper sulphide of some kind.

(b) Diffraction patterns from this sulphide phase were consistent with an f.c.c. mineral, a$\sim$3.6Å.

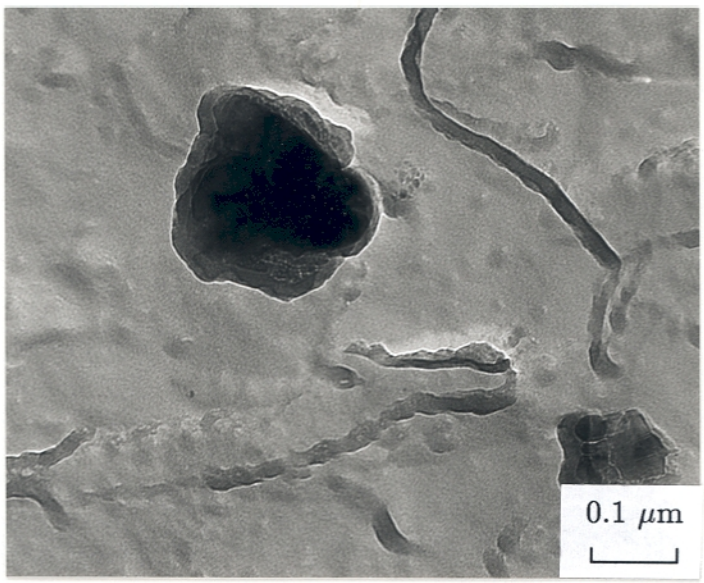

Figure 16 TEM micrograph showing the morphology typical of inclusions in Weld B. They are well rounded.

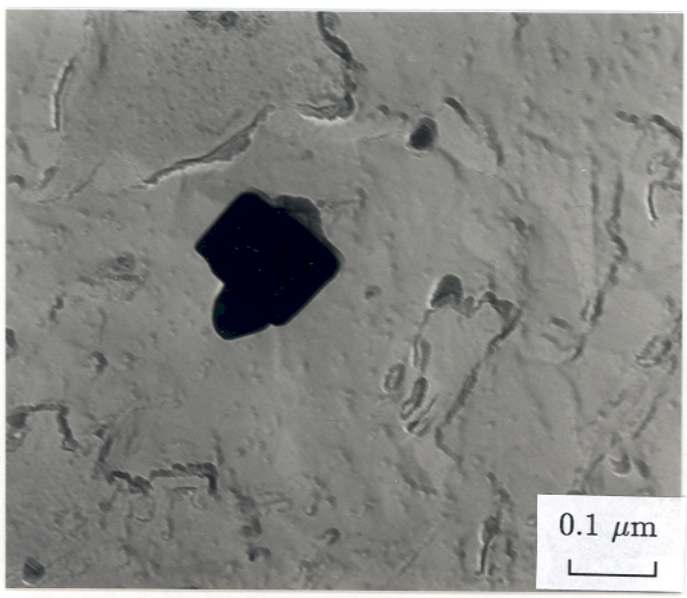

Figure 17 TEM micrograph showing more angular inclusions frequently observed in Weld C and Weld D.

TUNGSTEN–CONTAINING WELDS

Welds A, E, F and G contained systematic variations in tungsten. As already stated, Weld A was prepared using the unmodified flux (Table 2). Weld E was produced by addition of WO_3 powder to the flux; additions of W powder produced Weld F; FeW powder was added to the flux to produce Weld G. The compositions of the welds are shown in Table 6.

Weld no.	C	Si	Mn	W	Al	Ti	O	N
Weld A	0.075	0.36	1.26	0.014	0.012	0.003	280	48
Weld E	0.064	0.22	1.01	0.683	0.011	0.002	401	53
Weld F	0.075	0.41	1.24	1.479	0.014	0.004	314	81
Weld G	0.072	0.40	1.22	1.693	0.032	0.004	313	73

Table 6 Compositions of the tungsten weld series. Concentrations are given in wt.%, and O and N in parts per million by weight.

As–Deposited Microstructure

A cross–section of the top bead was examined using optical microscopy (Figures 18–21), which illustrates a continuous reduction in the amount of grain boundary nucleated phases with increasing tungsten content. The low tungsten welds, Weld A and Weld E, show considerable quantitites of allotriomorphic and Widmanstätten ferrite. In weld Weld F, the thickness of the allotriomorphic ferrite layers is greatly reduced, although Widmanstätten ferrite can still be seen.

The as–deposited microstructures show an increasing dominance of intragranular phases over grain boundary nucleated phases, with increasing tungsten. However, the reduction in allotriomorphic ferrite again implies hardenability changes as well as possible alterations in the inclusion potency.

The greater refinement of the as–deposited microstructure may therefore have occurred for two reasons:

(i) increased nucleation efficacy of inclusions which changed in chemistry/mineralogy as tungsten was added.

(ii) increased hardenability of the alloy due to tungsten present in solution.

Examination of Inclusions

Carbon extraction replicas were prepared from each of the top weld beads to characterise the inclusions. TEM EDX analysis was performed in order to investigate variations in the levels of tungsten present, as well as other potential chemical, and hence mineralogical differences between the inclusion populations. The work revealed the following:

(i) Tungsten was not detected in any of the one hundred and forty–seven particles examined. The experiments have not resulted in the incorporation of tungsten oxide in the welds. The tungsten is present in solid solution in the ferrite.
(ii) The chemical composition of the inclusions did not change much for the different welds (Figures 22–25). Some minor variations were found (*e.g.* manganese levels decrease while aluminium levels increase as the additions of tungsten increase), but were judged not to be of much consequence.

Diffraction patterns were taken when possible, during the collection of EDX microanalysis data. These showed the presence of γ-Al_2O_3 (Fig.26), TiX (where X=C, N or O, Fig.27), MnS (Fig.28), and a phase which indexed as f.c.c. with a$\sim$3.6Å. No obviously crystalline silicon–rich areas could be observed, presumably because of the presence of glass silicate.

Although the spatial and size distributions of the inclusions across the weld series were not measured quantitatively, no significant differences seemed apparent. Fig.29 a,b are from the high and low tungsten welds, and show that the inclusion sizes and spatial distributions are qualitatively similar. Further, no obvious inclusion morphological differences are apparent.

Hardenability Effect of Tungsten

Since different concentrations of tungsten present in the experimental welds produced no significant effects on the non–metallic inclusion populations, it is suspected that microstructural alterations have been produced due to the effects of tungsten in solution.

In order to demonstrate the hardenability effect of tungsten, standard thermomechanical specimens (cylinders of diameter 8 mm, and height 12 mm) were machined from weld metal of the low and high tungsten extremes of the weld series. These were austenitised at 1000°C for 5 mins before gas–quenching to room temperature. Radial dilatational information was recorded during the quench to determine the transformation kinetics.

Two different cooling rates were used to study transformations – 10 and 50°C s^{-1}. As the dilatational curves in Fig.30 a,b indicate, the onset of transformation was retarded

in the high tungsten samples. The onset temperatures for the two weld metals can be seen in Fig.31 a,b (high W ~690°C, low W ~720°C at 10 °C s^{-1}; high W ~530°C, low W ~580°C at 50°C s^{-1}). The hardenability of the alloy is clearly increased by tungsten in solution.

Optical micrographs of the microstructures produced by these gas–quench experiments are shown in Figures 32 and 33. There is more martensite in the high tungsten alloy, as would be expected from its greater hardenability.

CONCLUSIONS

Variations in levels of titanium and tungsten in experimental submerged arc welds have been achieved by the addition of various powders to a standard welding flux. Increasing titanium has caused a general increase in intragranular as opposed to grain-boundary phases in the as–deposited weld microstructure. The microstructural changes have arisen due to an apparent dual effect of titanium:

(i) Increases in titanium have caused increases in Ti–rich minerals in the non–metallic inclusions. This has been associated with an increased efficacy for nucleating acicular ferrite.

(ii) For large levels of titanium, such as in Weld C and Weld D, much of the titanium remains in solution. This seems to cause increased alloy hardenability.

Increasing tungsten has also caused a general increase in acicular ferrite. However, tungsten is not involved as a cation in the non–metallic inclusions. Instead, microstructural refinement has occurred due to hardenability effects of tungsten in solution.

ACKNOWLEDGMENTS

The authors are grateful to the Education Department (N. Ireland) and ESAB SWEDEN for financial support and to Professor Colin Humphreys for the provision of laboratory facilities at the University of Cambridge. HKDHB's contribution was under the auspices of the "Atomic Arrangements: Design and Control Project" which is a collaborative venture between the University of Cambridge and the Research and Development Corporation of Japan.

REFERENCES

1. J. M. Gregg and H. K. D. H. Bhadeshia: *Acta Metallurgica* **42** (1994) 3321–3330
2. J. M. Gregg and H. K. D. H. Bhadeshia: *Metallurgical and Materials Transactions A* **25A** (1994) 1603–1611
3. J. M. Gregg and H. K. D. H. Bhadeshia: *'Solid-State Nucleation of Acicular Ferrite on Minerals Added to Molten Steel'* (1995) unpublished

4 . A. O. Kluken and Ø. Grong: *Metallurgical Transactions A* **20A** (1989) 1335–1349

5 . H. K. D. H. Bhadeshia and L-E Svensson: *Mathematical Modelling of Weld Phenomena* (1993) 109–212

6 . T. B. Massalki: *Binary Alloy Phase Diagrams* (1986) 1118

7 . D. J. Widgery: *American Welding Journal* (1976) 57-s–68-s

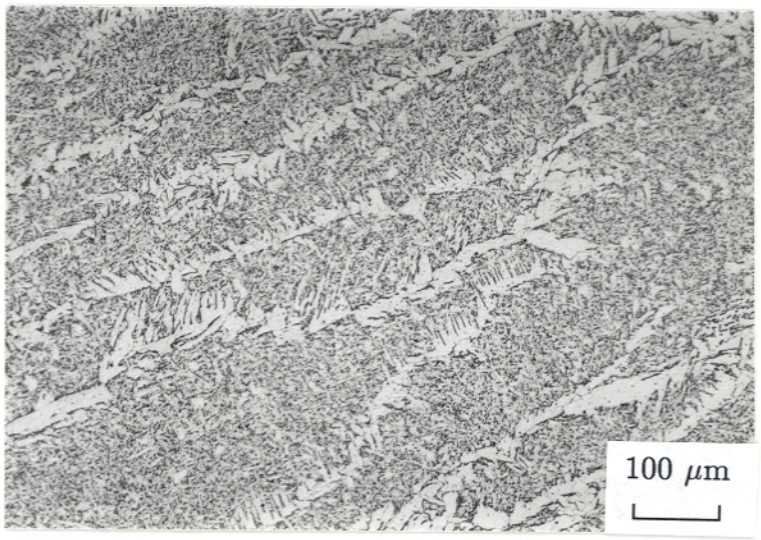

Figure 18 Optical micrograph of the as–deposited microstructure of Weld A (the lowest tungsten addition).

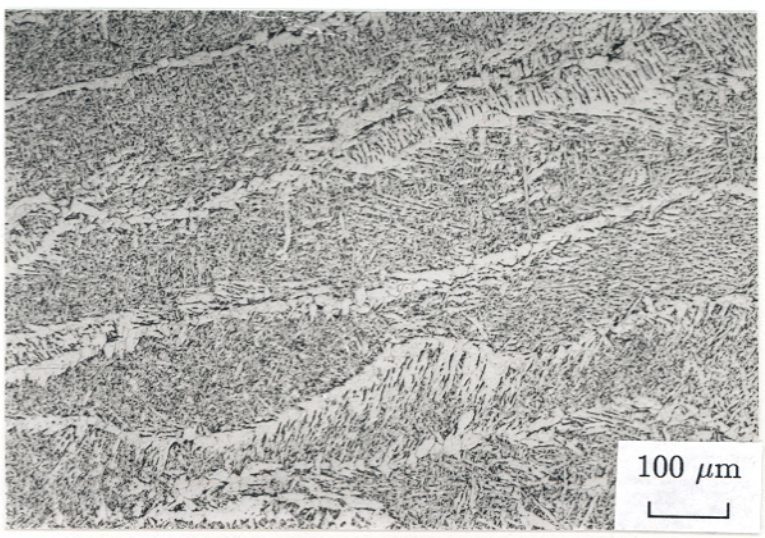

Figure 19 Optical micrograph of the as–deposited microstructure of weld Weld E.

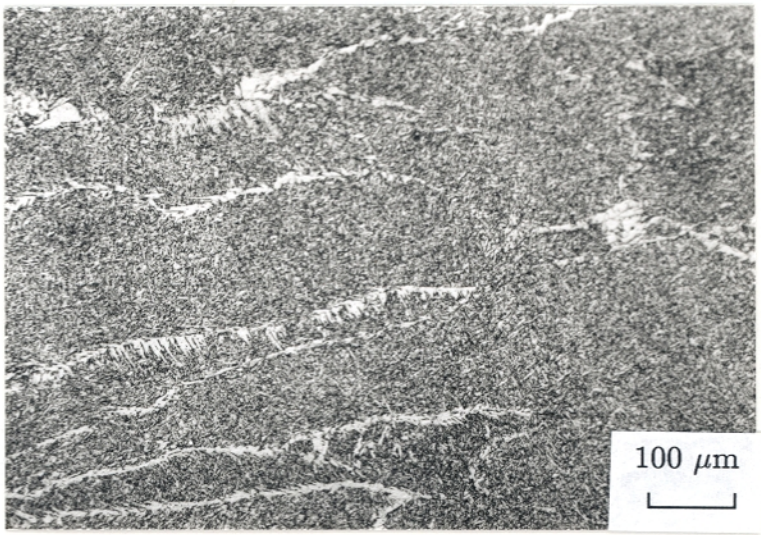

Figure 20 Optical micrograph of the as–deposited microstructure of weld Weld F.

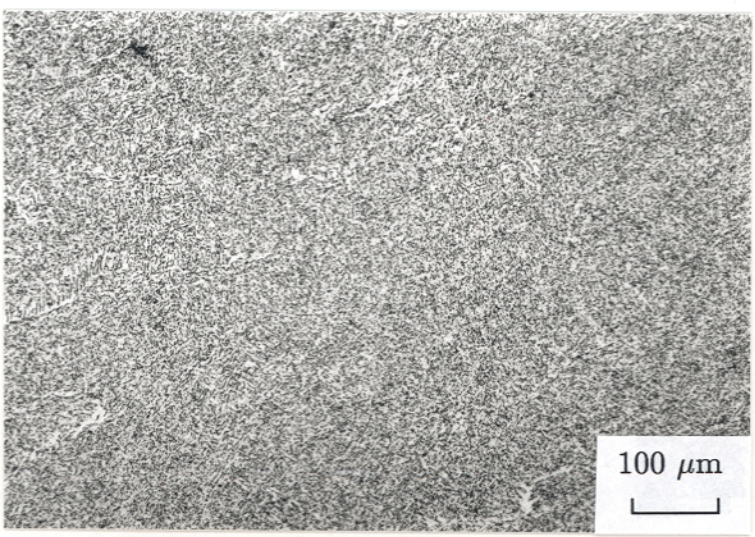

Figure 21 Optical micrograph of the as–deposited microstructure of weld Weld G (the most tungsten rich of the weld series).

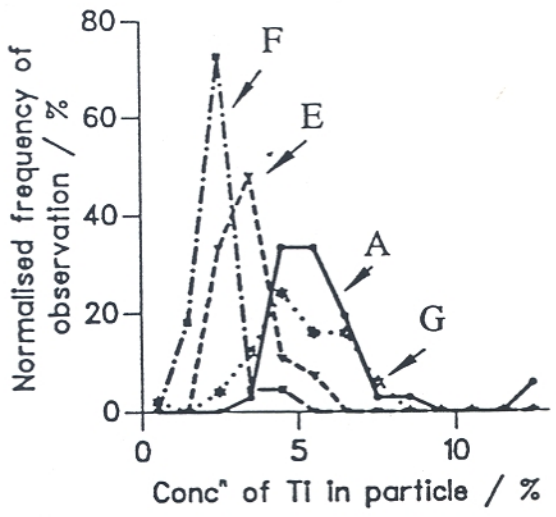

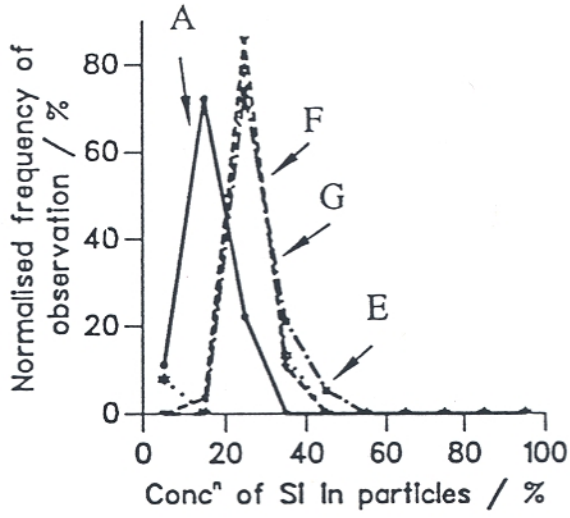

Figure 22 (left) Titanium concentration distributions in the inclusions across the tungsten–weld series. Concentrations are in wt% .
Figure 23 (right) Silicon concentration distributions in the inclusions across the tungsten–weld series. Concentrations are in wt% .

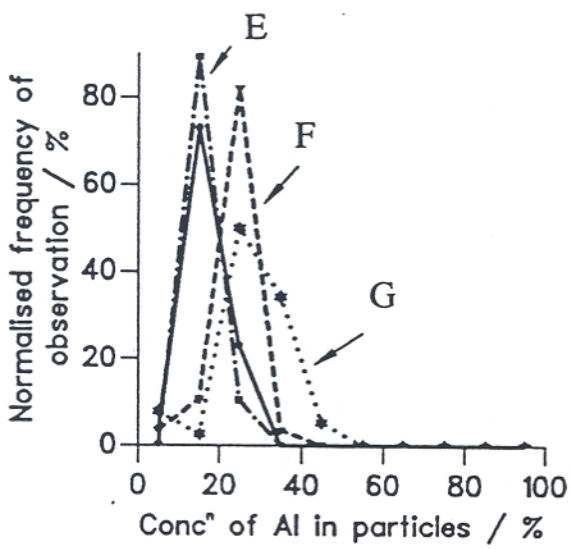

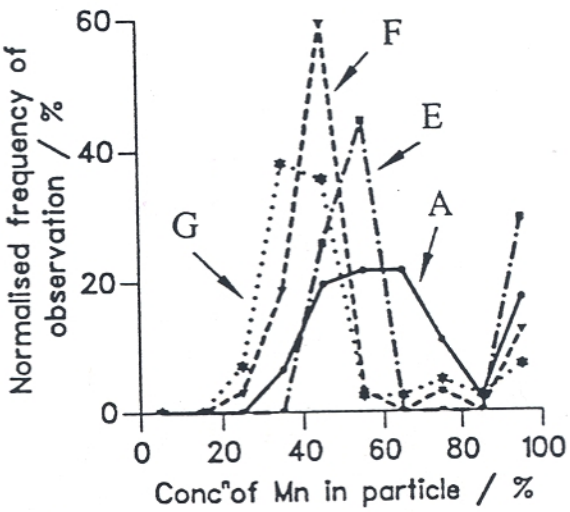

Figure 24 (left) Aluminium concentration distributions in the inclusions across the tungsten–weld series. Concentrations are in wt% .
Figure 25 (right) Manganese concentration distributions in the inclusions across the tungsten–weld series. Concentrations are in wt% .

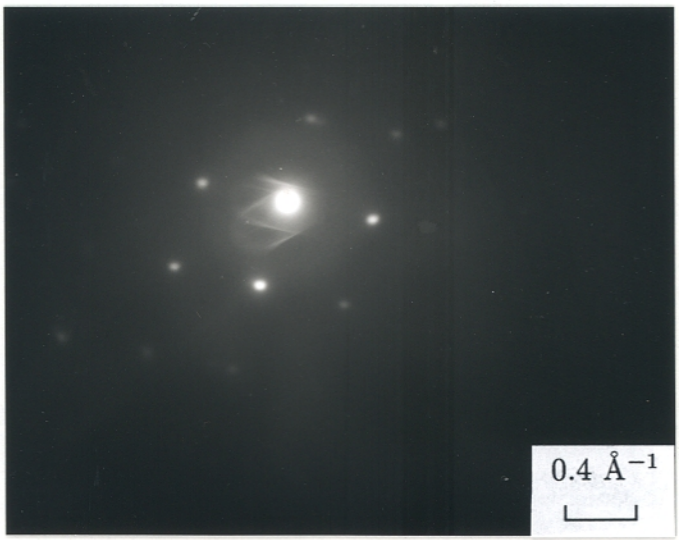

Figure 26 Diffraction patterns taken from strongly diffracting inclusions, found during EDX analysis, showed the presence of various minerals. This pattern illustrates the presence of γ-Al_2O_3.

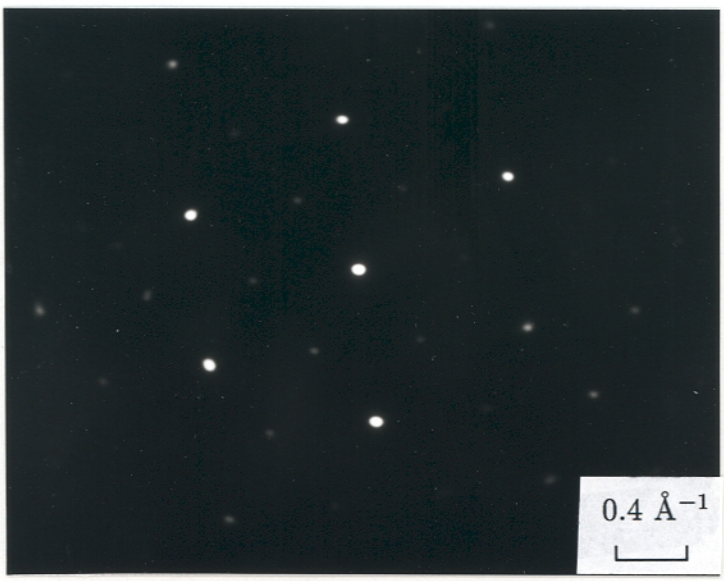

Figure 27 Diffraction patterns consistent with a TiX phase were obtained.

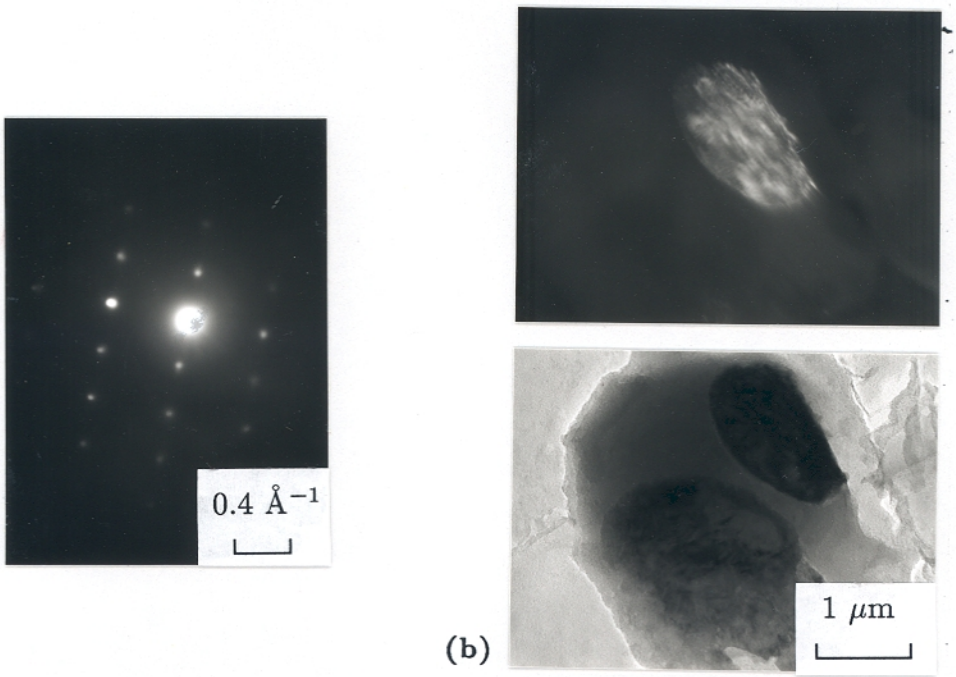

Figure 28 (a) Diffraction consistent with MnS was obtained in inclusions across the weld series.

(b) Dark and bright field micrographs of the MnS regions within one inclusion. This illustrates the inhomogeneous, multicrystalline nature of real weld inclusions.

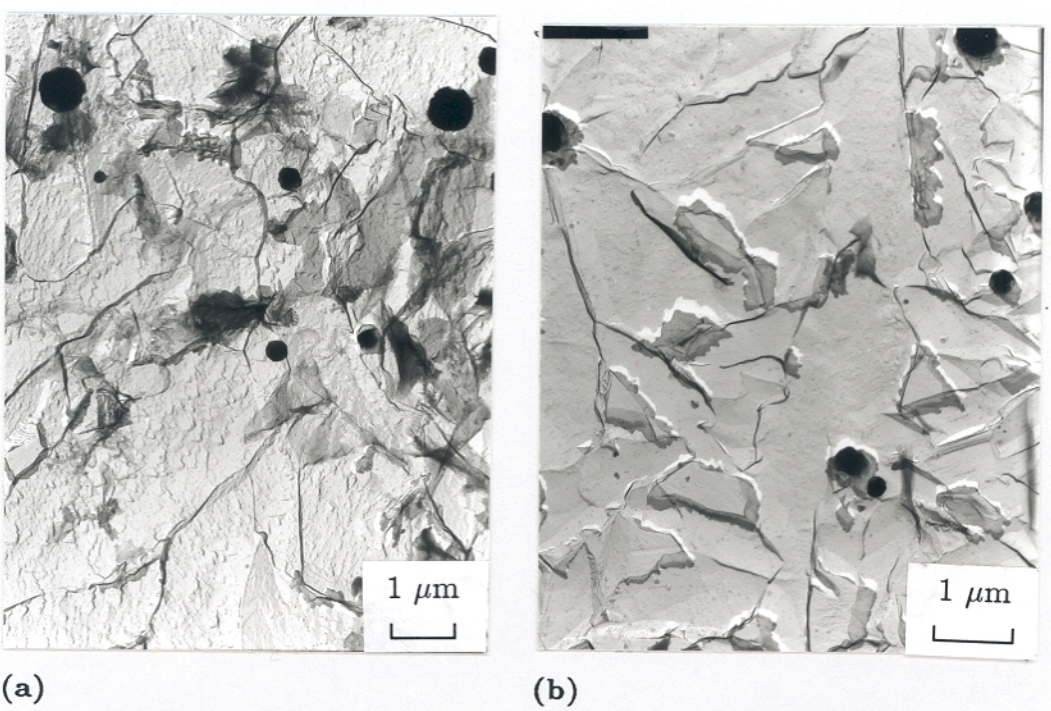

Figure 29 (a) TEM bright field micrograph showing the qualitative size and distribution of inclusions in Weld A.

(b) TEM bright field micrograph showing the qualitative size and distribution of inclusions in weld Weld G.

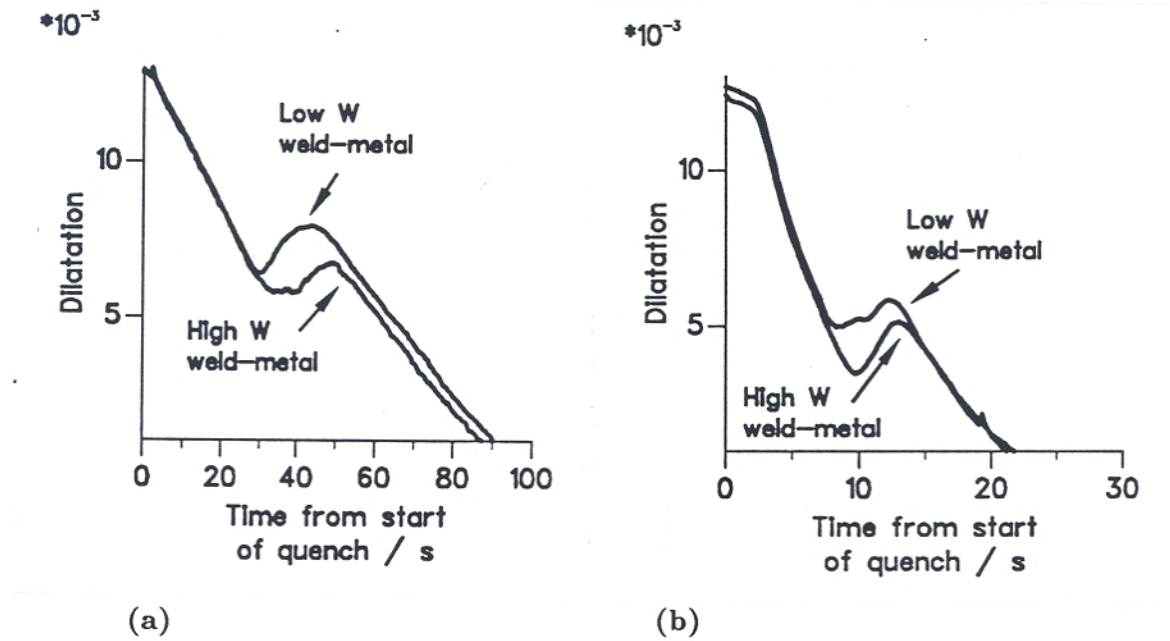

(a) (b)

Figure 30 (a) Dilatation curves obtained during the gas–quenching of weld metal Weld A and Weld G (low and high tungsten respectively) at $10°C\,s^{-1}$.

(b) Dilatation curves obtained for gas–quenching at $50°C\,s^{-1}$.

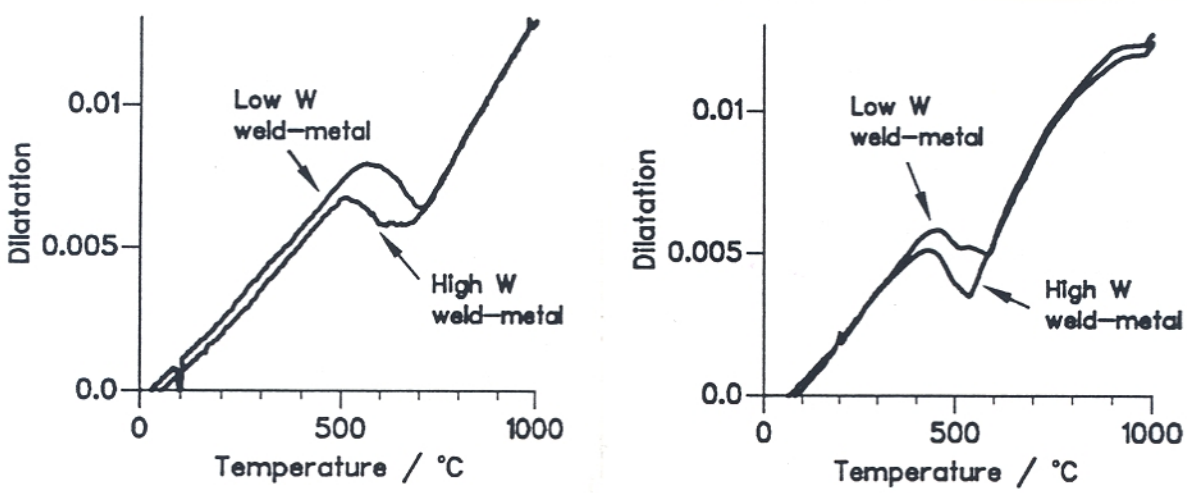

(a) (b)

Figure 31 (a) Dilatation curves obtained during gas–quenching at $10°C\,s^{-1}$, illustrating the differences in temperatures at which tranformation was initially observed.

(b) Dilatation curves showing the onset temperatures of transformation during gas–quench of $50°C\,s^{-1}$.

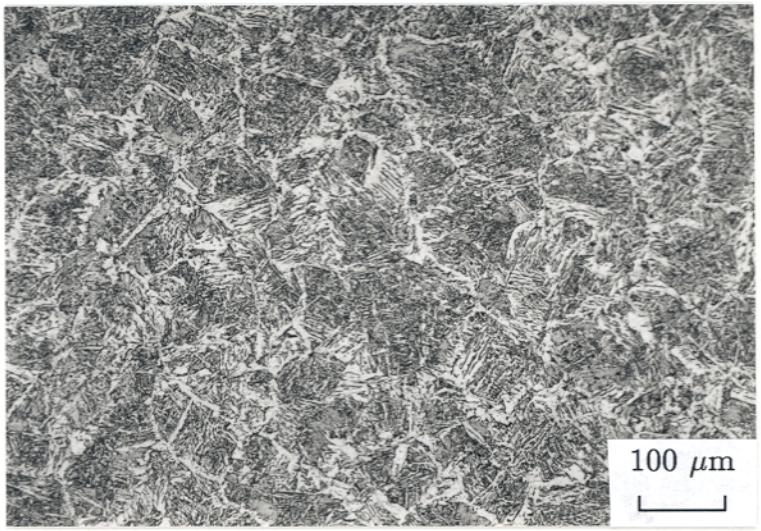

Figure 32 Optical micrograph of the microstructure of the low tungsten weld (Weld A) after quenching at $50°C\,s^{-1}$ from 1000°C.

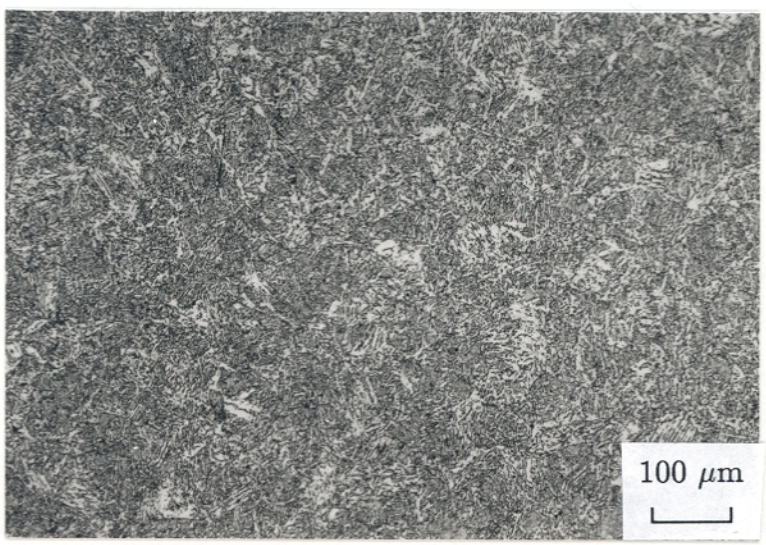

Figure 33 Optical micrograph of the microstructure of the high tungsten weld (Weld G) after quenching at $50°C\,s^{-1}$ from 1000°C. There is more martensite apparent in the high tungsten alloy, illustrating its greater hardenability.